Research Article

Nano Research
2021, 14(5): 1374–1381

ISSN 1998-0124 CN 11-5974/O4
https://doi.org/10.1007/s12274-020-3186-x

Atomic Fe-Zn dual-metal sites for high-efficiency pH-universal oxygen reduction catalysis

Jie Xu[1,§], Shuhua Lai[1,§], Defeng Qi[1], Min Hu[1], Xianyun Peng[1], Yifan Liu[2] (✉), Wei Liu[1], Guangzhi Hu[3], Heng Xu[1], Fan Li[1], Chao Li[1], Jia He[1] (✉), Longchao Zhuo[4], Jiaqiang Sun[5], Yuan Qiu[1], Shusheng Zhang[6], Jun Luo[1], and Xijun Liu[1] (✉)

[1] *Institute for New Energy Materials & Low-Carbon Technologies and Tianjin Key Lab of Photoelectric Materials & Devices, School of Materials Science and Engineering, Tianjin University of Technology, Tianjin 300384, China*
[2] *College of Physics and Optoelectronic Engineering, Shenzhen University, Shenzhen 518060, China*
[3] *Institute for Ecological Research and Pollution Control of Plateau Lakes, School of Ecology and Environmental Science, Yunnan University, Kunming 650504, China*
[4] *School of Materials Science and Engineering, Xi'an University of Technology, Xi'an 710048, China*
[5] *State Key Laboratory of Coal Conversion, Institute of Coal Chemistry, Chinese Academy of Sciences, Taiyuan 030001, China*
[6] *College of Chemistry, Zhengzhou University, Zhengzhou 450000, China*
[§] *Jie Xu and Shuhua Lai contributed equally to this work.*

Received: 21 August 2020 / **Revised:** 12 October 2020 / **Accepted:** 17 October 2020

ABSTRACT

An effective electrocatalyst being highly active in all pH range for oxygen reduction reaction (ORR) is crucial for energy conversion and storage devices. However, most of the high-efficiency ORR catalysis was reported in alkaline conditions. Herein, we demonstrated the preparation of atomically dispersed Fe-Zn pairs anchored on porous N-doped carbon frameworks (Fe-Zn-SA/NC), which works efficiently as ORR catalyst in the whole pH range. It achieves high half-wave potentials of 0.78, 0.85 and 0.72 V in 0.1 M $HClO_4$, 0.1 M KOH and 0.1 M phosphate buffer saline (PBS) solutions, respectively, as well as respectable stability. The performances are even comparable to Pt/C. Furthermore, when assembled into a Zn-air battery, the high power density of 167.2 $mW \cdot cm^{-2}$ and 120 h durability reveal the feasibility of Fe-Zn-SA/NC in real energy-related devices. Theoretical calculations demonstrate that the superior catalytic activity of Fe-Zn-SA/NC can be contributed to the lower energy barriers of ORR at the Fe-Zn-N_6 centers. This work demonstrates the potential of Fe-Zn pairs as alternatives to the Pt catalysts for efficient catalytic ORR and provides new insights of dual-atom catalysts for other energy conversion related catalytic reactions.

KEYWORDS

Fe-Zn atomic pairs, oxygen reduction reaction, pH-universal, Zn-air battery, electrocatalysis

1 Introduction

Electrochemical oxygen reduction reaction (ORR) has attracted wide attention due to its significance in energy conversion and storage, such as fuel cells and metal-air batteries [1–5]. The catalysts for high-efficiency ORR are considered to be the key obstacles that limiting their application towards practical devices [6–12]. Platinum (Pt)-based catalysts have been studied for decades due to their high catalytic activity toward ORR. However, their large-scale applications are limited by their prohibitive price and limited stability [13–15].

In recent years, single-atom catalysts in the form of metal-nitrogen doped carbon (M-NC, M = Fe, Co, Ni, etc.) have been proposed as the most promising alternatives to Pt-based catalysts for ORR [16–24] due to their excellent catalytic ability, maximized atom efficiency, tunable electronic properties and more exposed active sites [25–28]. Generally, the metal single atoms are recognized as active centers for ORR catalysis, and the nitrogen atoms not only act as anchoring sites to stabilize the metal atoms but also can regulate the electronic structures of metal centers [2, 29, 30]. However, these single-atom electrocatalysts are always reported with excellent ORR activity exclusively in alkaline electrolyte [31, 32]. Considering that in some cases of the energy devices, like polymer electrolyte membrane fuel cells and biofuel cells, acidic or neutral electrolytes are needed, the narrow pH range ORR catalysts worked greatly hindered their applicability and universality in energy conversion and storage [33]. Improving the ORR electrocatalytic activity of these atomic metal catalysts in acidic and neutral electrolytes is urgently needed. Recently, Lu et al. reported Zn-Co atomic pairs catalyst delivers excellent catalytic activity for ORR in both acidic and alkaline electrolyte [34]. N-coordinated Fe-Co dual sites were also reported to deliver outstanding activity for ORR in acidic electrolyte [35]. More importantly, these catalysts all show that the atomic pair sites composed of different types of metals can further enhance the ORR catalytic activity through the "synergistic effect" between the isolated metal sites on carbon matrix. Those works inspired us that the ORR catalytic activity of atomic catalysts would be enhanced and can be expanded into a wider pH range by

Address correspondence to Yifan Liu, liuyifan@szu.edu.cn; Jia He, hejia@tjut.edu.cn; Xijun Liu, xjliu@tjut.edu.cn

employing bimetallic atomic catalysts as active sites.

Herein, we designed an efficient synthesis route to prepare atomically dispersed Fe-Zn pairs anchored on porous N-doped carbon frameworks (Fe-Zn-SA/NC) as an efficient catalyst for ORR. The as-synthesized isolated Fe-Zn pairs are clearly identified through electron energy-loss spectroscopy (EELS) and are determined to be bonded with six pyridinic-N atoms (Fe-Zn-N_6) in the surroundings carbon matrix by synchrotron-radiation X-ray absorption fine structure spectroscopy (XAFS). Furthermore, the porous nature of the carbon support ensures abundant exposed active sites and efficient transfer of the ORR-related electrons, which endows Fe-Zn-SA/NC with excellent ORR activities in all-over pH range. It exhibits ultrahigh half-wave potentials ($E_{1/2}$) of 0.78, 0.85 and 0.72 V in 0.1 M $HClO_4$, 0.1 M KOH and 0.1 M phosphate buffer saline (PBS), respectively, all of which are very close to that of Pt/C and comparable with the most reported ORR catalysts (Tables S1–S3 in the ESM). In addition, The density functional theory calculation (DFT) demonstrates that the relatively lower energy barriers at the Fe-Zn-N_6 centers towards ORR contribute to its high ORR catalytic activity. This work not only demonstrated the novel synthesis of Fe-Zn atomic catalyst, but also gave the first example for an atomic pair catalyst toward effective ORR in all-pH range.

2 Experimental

2.1 Synthesis of Fe-Zn-SA/NC

The Fe-Zn-SA/NC was synthesized by a simple calcination method. In details, 0.432g glucose ($C_6H_{12}O_6$), 5.17g NH_3OHCl, 0.837 mg (ca. 150 μL) of $C_{12}H_{22}O_{14}Fe{\cdot}2H_2O$ aqueous solution (0.0125 mol/L) and 0.341 mg of (ca. 200 μL) $ZnCl_2$ aqueous solution (0.0125 mol/L) were ultrasonically dispersed in an 80 mL water-ethanol solution (the volume ratio of 1:1) for 30 min. A uniform solution was formed without any sediments. After that, the mixture was dried directly at 60 °C overnight by an air circulation oven to evaporate the redundant solvents, and the residual precipitated solid powder was collected. Subsequently, it was transferred into a tube furnace and purged with pure Ar (99.9%) for 30 min to get an inert atmosphere. Then, the prepared samples were heated to 950 °C at a rate of 5 °C·min^{-1} and kept for 4 h. Next, they were cooled down naturally. The whole procedure was conducted under a constant Ar flow.

2.2 Synthesis of Fe-SA/NC and Zn-SA/NC

The Fe-SA/NC and Zn-SA/NC were synthesized by similar synthesis steps with that of Fe-Zn-SA/NC, except for solely adding 1.952 mg (ca. 350 μL) of $C_{12}H_{22}O_{14}Fe{\cdot}2H_2O$ aqueous solution for Fe-SA/NC and 0.596 mg (ca. 350 μL) $ZnCl_2$ aqueous solution for Zn-SA/NC, respectively. It is worth noting that the mole amount of Fe or Zn in Fe-SA/NC and Zn-SA/NC is equal to the total amount of Fe and Zn in Fe-Zn-SA/NC.

2.3 Synthesis of NC

The NC was synthesized through a synthesis procedure similar to Fe-Zn-SA/NC, except that $C_{12}H_{22}O_{14}Fe{\cdot}2H_2O$ and $ZnCl_2$ were not added.

2.4 Physical characterization of materials

The X-ray diffraction (XRD) patterns were collected by an X-ray diffractometer (Rigaku SmartLab 9 kW) at a scan rate of 20 °·min^{-1} from 10° to 90° with Cu Kα radiation (λ = 0.154598 nm). The morphologies and microstructures of the prepared samples were characterized by using a field emission gun scanning electron microscopy (SEM) instrument (Verios 460L of FEI), and the high-resolution transmission electron microscope (HRTEM, FEI Talos F200X S/TEM) with a field-emission gun at 200 kV. In addition, the atomic-resolution high-angle annular dark-field scanning transmission electron microscopy (HAADF-STEM) images, EELS spectra and energy-dispersive X-ray spectroscopy (EDS) mappings were recorded with the aberration-corrected scanning transmission electron microscopy (AC-STEM, FEI Titan Cubed Themis G2 300) at 200 kV with a probe corrector and a monochromator. The X-ray photoelectron spectroscopy (XPS) characterizations were performed by a Thermo Scientific K-alpha XPS system (Thermo Fisher Scientific, UK) with the Al Kα radiation as the X-ray source. The hard XAS measurements on the Fe and Zn K-edge were carried out in the fluorescence mode of 4B9A beamline of Beijing Synchrotron Radiation Facility (BSRF). The Raman spectrum was recorded on a Horiba Evolution (Horiba, France) Raman microscope. Furthermore, the concentration of Fe and Zn species was determined by the inductively coupled plasma-atomic emission spectroscopy (ICP-AES, SPECTRO-BLUE). The adsorption and desorption isotherms of N_2, as well as the pore size distribution curve, were measured with an Autosorb-iQ-MP Micromeritics analyzer at 77 K.

2.5 Electrochemical measurements

The preparation methods of the working electrode catalyst are as follows: first, the catalyst ink was prepared by mixing 6 mg of the catalysts (such as Fe-Zn-SA/NC) with a solution containing 450 μL of anhydrous ethanol, 500 μL of H_2O and 50 μL of 5% Nafion solution, and the mixed solution was then ultrasonically treated for 30 min to obtain a uniformly dispersed liquid. Then, 20 μL of the well-dispersed catalyst ink was coated on the polished glassy carbon rotating disk electrode (RDE) or rotating ring disk electrode (RRDE) to yield an absolute mass loading of 0.6 mg·cm^{-2}. Commercial 20 wt.% Pt/C was also prepared by dispersing 6 mg of the catalyst in 1 mL of the above-mentioned similar solution. The mass ratio of Pt/C, Fe-SA/NC, Zn-SA/NC and NC is similar to that of Fe-Zn-SA/NC catalyst.

All electrochemical measurements were carried out using the CHI Electrochemical Station (760E) of the three-electrode system. We used Pt foil and Hg/HgO was used as a counter electrode and reference electrode, and all electrochemical tests were performed at 25 °C in 0.1 M KOH, 0.1 M $HClO_4$ and 0.1 M PBS, respectively. Before ORR electrochemical test, the electrolyte was first saturated with O_2 for 30 min, and the flow rate was kept constant during the subsequent measurements. Similarly, before the test, the cyclic voltammetry (CV) method was used to activate the catalysts with a scan rate of 100 mV·s^{-1} between 0.1–1.1 V versus reversible hydrogen electrode (vs. RHE). The linear sweep voltammetry (LSV) curves were recorded by varying the scanning voltage on the cathode from 1.23 to 0.1 V. The measurements of RDE and RRDE were obtained at a rotating speed of 1,600 rpm with a sweep rate of 10 mV·s^{-1}. All of the measured potentials of catalyst were referenced to the RHE according to the Nernst equation potential

$$E_{RHE}\ (V) = E_{Hg/HgO}\ (V) + 0.0591 \times pH + 0.098\ (V)$$

For ORR of RDE, the electron transfer number (n) was analyzed based on the Koutecky-Levich (K-L) equation [22]

$$\frac{1}{J} = \frac{1}{J_L} + \frac{1}{J_K} = \frac{1}{Bw^{1/2}} + \frac{1}{J_K}$$

$$B = 0.62nFC_0D_0^{2/3}\theta^{-1/6}$$

$$J_K = nFkC_0$$

where J is the measured current density; the J_L and J_K is the limiting current and kinetic densities, respectively; ω is the angular velocity of the disk; n is the numbers of electron transferred in the ORR; F is the Faraday constant (96,485 C·mol^{-1}); C_0 is the bulk concentration of O_2 (1.2×10^{-6} mol cm^{-3}); D_0 is the diffusion coefficient of O_2 (1.9×10^{-5} cm^2·s^{-1}); θ is the kinematic viscosity of the electrolyte (0.01 cm^2·s^{-1}); and k is the electron transfer rate constant. In addition, the hydrogen peroxide yield (H_2O_2%) and the electron transfer number (n) were also calculated through the RRDE technique. During the entire test, the disk electrode was scanned at a speed of 10 mV·s^{-1} and the ring electrode potential was set to 1.20 V vs. RHE. H_2O_2% and n of catalyst were determined by the following equations [22]

$$H_2O_2(\%) = 200 \times \frac{\frac{I_r}{N}}{\frac{I_r}{N} + I_d}$$

$$n = 4 \times \frac{I_d}{I_d + \frac{I_r}{N}}$$

where I_d and I_r are the disk and ring current, respectively, and N is the current collection efficiency of the Pt ring, which is 0.37 in this test. We further determined the electrochemical active surface area (ECSA) of different catalysts based on the double-layer capacitance (C_{dl}) values that were obtained by CV measurements in a non-Faradaic resign at different scan rates from 10 to 30 mV·s^{-1}. Electrochemical impedance spectroscopy (EIS) was performed in the frequency range from 1,000 kHz to 10 mHz with a voltage amplitude of 5 mV.

2.6 Zn-air battery fabrication

The primary Zn-air batteries were tested with a home-built three-electrode device. The whole-cell consists of anode, cathode and electrolyte. The cathode (i.e., the air electrode) was made by nickel foam, catalyst layer and gas diffusion layer. It should be noted that the catalyst side of the air electrode should be placed in direct contact with air. The air electrode was made as follows: firstly, the homogeneous catalyst ink such as Fe-Zn-SA/NC and 20 wt.% Pt/C was prepared by mixing and stirring expandable graphite, activated carbon, and polytetrafluoroethylene (PTFE) (60 wt.% PTFE emulsion dispersed in water), wherein their mass ratio is 3:3:3:1. The cathode was prepared through dropping the catalyst ink onto nickel foam of (2 cm × 2 cm) with a loading of 2 mg·cm^{-2}, and dried at 60 °C for 12 h for later use. The gas diffusion layer consists of camphor, acetylene black (10 wt.%), PTFE (25 wt.%) and polyvinylidene fluoride (PVDF, 45 wt.%). The 5 mm polished Zn foil was used as the anode. 0.2 M zinc acetate + 6 M KOH aqueous solution and 4 mol·L^{-1} NH_4Cl + 1 mol·L^{-1} KCl aqueous solution was utilized as the electrolyte for alkaline and neutral Zn-air batteries, respectively. The discharge performance of the battery was tested under chronopotentiometry program (CHI 760E, China).

2.7 Computational details

First-principles computations are performed using the DMol^3 code. The Perdew-Burke-Ernzerhof (PBE) exchange-correlation functional within a generalized gradient approximation (GGA) was employed. The double numerical plus polarization (DNP) was chosen as the basis set for other elements. To ensure high-quality results, self-consistent field (SCF) calculations were performed with a convergence criterion of $2.0 \times e^{-5}$ and the cutoff radius of the real space global orbit was chosen as high as 4.5 Å.

3 Results and discussion

As depicted in Fig. 1(a), the isolated Fe-Zn atomic pairs on N-doped carbons were synthesized by a simple calcination method. The HRTEM image in Fig. 1(b) and Fig. S1(a) in the Electronic Supplementary Material (ESM) also show the carbon substrate lattice with an interplanar distance of 0.342 nm for the (002) facets of graphitic carbon, which is in agreement with the typical (002) peak of graphitic carbon phase by the XRD pattern (Fig. S1(b) in the ESM) [36]. STEM images in Fig. 1(c) and Fig. S2 in the ESM indicate that there are many defect pores on the surface of the Fe-Zn-SA/NC, which is caused by volatilization of the gas generated during high-temperature calcination. In addition, the N_2 physisorption isotherms for Fe-Zn-SA/NC suggest that the coexistence of mesopores and micropores with an ultrahigh specific surface area of 810.66 m^2·g^{-1} (Fig. S3 in the ESM). Raman spectra (Fig. S4 in the ESM) also suggest that many structural defects are produced on the N-doped carbon support [37]. The mesopores and micropores defects are beneficial to the accessibility of active sites and the rapid transportation of ORR-relevant species during electrocatalysis. Furthermore, EDS elemental mapping in Fig. 1(d) reveals that the C, N, Fe and Zn elements are homogeneously distributed over the entire flakes. Besides, the uniformly distributed N element tends to form N-doped carbons, like graphitic-N, which would modulate the electronic properties of graphene and contribute to the enhanced electron transfer during electrocatalysis [35, 38]. More importantly, DFT calculation results also show that Fe-Zn metal sites are more likely to exchange electrons with the carbon matrix after N-doping (Fig. S5 in the ESM). To identify the form of the Fe and Zn atoms distributed on N-doped carbon supports, the aberration-corrected HAADF-STEM was performed [39–41]. As shown in Fig. 1(e) (additional enlarged images are shown in Fig. 1(f)), isolated heavier Fe or Zn single atoms and some Fe-Zn atomic pairs are distributed all over the porous N-doped carbon framework. More importantly, they can be accurately identified by EELS in Fig. 1(g) (raw data in Fig. S6 in the ESM).

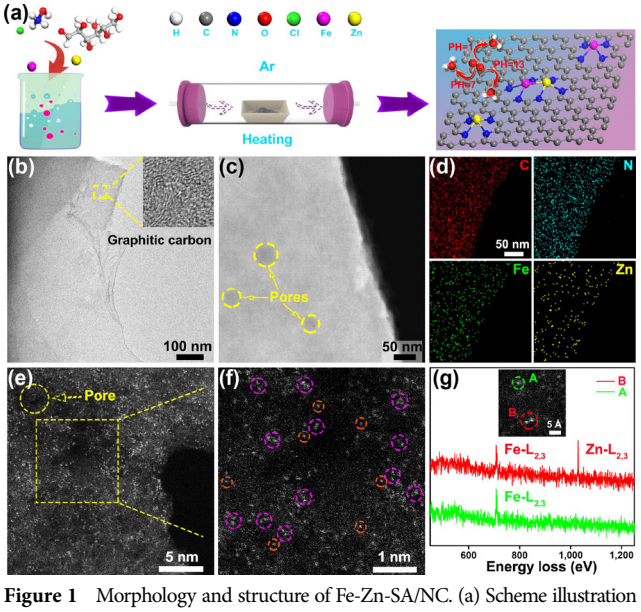

Figure 1 Morphology and structure of Fe-Zn-SA/NC. (a) Scheme illustration for the synthesis. (b) HRTEM image. (c) Low-magnification HAADF-STEM image. (d) EDS mappings of the corresponding C, N, Fe and Zn. The images have the same scale bars. (e) Atomic resolution HAADF-STEM image and enlarged images (f) of the Fe-Zn-SA/NC. In (f), some of Fe-Zn atomic pairs are highlighted by larger magenta circles, and some of single Fe or Zn atoms highlighted by smaller orange circles. (g) The EELS spectra of Fe-Zn-SA/NC.

The Fe-$L_{2,3}$ edge (710.0 eV) and Zn-$L_{2,3}$ edge (1,029.1 eV) were simultaneously detected on an atomic pair [42, 43], which can clearly prove the existence of Fe-Zn atomic pairs in the Fe-Zn-SA/NC. The Fe and Zn contents were measured to be 0.22 wt.% and 0.10 wt.% in the Fe-Zn-SA/NC, respectively, by ICP-AES. Furthermore, we also prepared Fe or Zn single atoms anchored to N-doped carbon (namely Fe-SA/NC and Zn-SA/NC), and N-doped carbon (denoted as NC) for comparison (Figs. S7–S9 in the ESM).

To gain deep insight into the surface chemical composition and elemental bonding configuration information of the Fe-Zn-SA/NC catalysts, the XPS was performed. Figure 2(a) shows the Fe 2p spectrum of Fe-Zn-SA/NC. Five peaks of 710.5, 712.8, 717.5, 723.6 and 725.3 eV are assigned to Fe^{2+} $2p_{3/2}$, Fe^{3+} $2p_{3/2}$, satellite peak, Fe^{2+} $2p_{1/2}$ and Fe^{3+} $2p_{1/2}$ on the basis of binding energies, respectively [44]. In the XPS spectrum of Zn 2p (Fig. 2(b)), the peaks at 1,021.8 and 1,044.8 eV correspond to the Zn^{2+} [37]. Additionally, in Fig. S10 in the ESM of the N 1s XPS spectrum, the presence of Fe–N bond (398.7 eV) and Zn–N bond (399.7 eV) further confirms that the Fe and Zn single sites in Fe-Zn-SA/NC are stabilized by N atoms [37, 45]. Of note, even that the boiling point of metal Zn is 907 °C, while the formation of Zn-N_4 bonds in Zn single-atoms prevents them from evaporating [46, 47]. To further investigate the Fe and Zn atomic configurations in Fe-Zn-SA/NC, we performed K-edge X-ray absorption near-edge structure (XANES) and extended X-ray absorption fine structure (EXAFS) tests. The Fe K-edge XANES spectra for Fe-Zn-SA/NC, along with Fe Foil and Fe_2O_3 references, were shown in Fig. 2(c). It indicates that the average valence of Fe atom is between Fe^{2+} and Fe^{3+}, which is consistent with the XPS analysis in Fig. 2(a). The Fourier transform (FT) κ^3-weighted EXAFS spectrum of Fe-Zn-SA/NC in Fig. 2(d) reveals the two prominent peaks

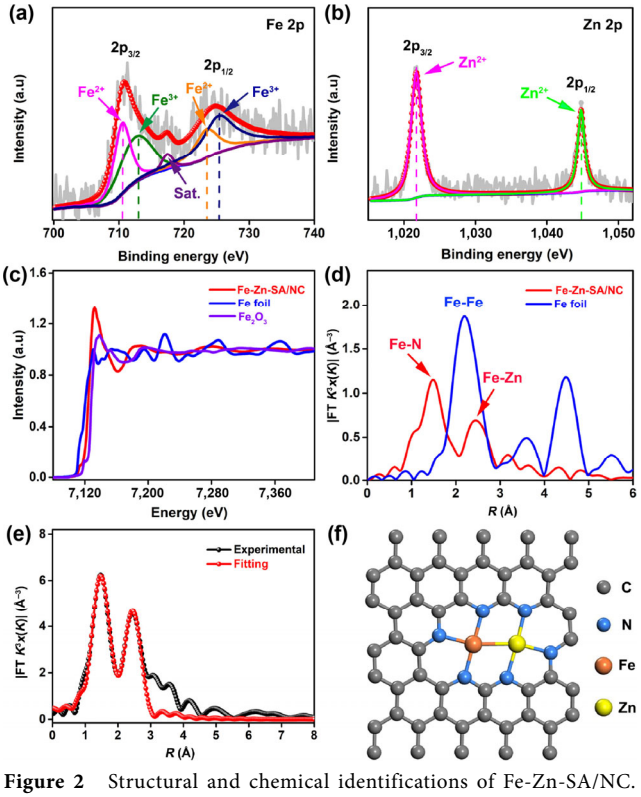

Figure 2 Structural and chemical identifications of Fe-Zn-SA/NC. (a) and (b) The high-resolution XPS Fe 2p and Zn 2p spectra of Fe-Zn-SA/NC. (c) and (d) Fe K-edge XANES and Fourier-transform EXAFS spectra of Fe-Zn-SA/NC and reference samples. (e) The quantitative EXAFS fitting curves of *R* space and the corresponding schematic model (f) of Fe-Zn-SA/NC.

located at 1.5 and 2.45 Å, which can be attributed to the Fe–N and Fe–Zn structure, respectively [30, 48]. These results are also consistent with N 1s XPS analyses in Fig. S10 in the ESM. It should be mentioned that the Fe–Fe coordination peak at 2.2 Å is not detected on Fe-Zn-SA/NC, revealing the atomic dispersion nature of Fe [48]. The quantitative EXAFS fitting was conducted to further identify the local coordination environment of Fe atom in Fe-Zn-SA/NC. The results are shown in Fig. 2(e). The fitting curves and analysis suggest that the Fe and Zn atoms in Fe-Zn-SA/NC are coordinated by six N atoms (Fig. 2(f)).

The ORR activity of Fe-Zn-SA/NC was first studied using a RDE in an O_2-saturated acidic electrolyte (0.1 M $HClO_4$). For comparison, a commercial Pt/C catalyst (20% Pt), Fe-SA/NC, and Zn-SA/NC were evaluated. As shown in Fig. S11 in the ESM, the CV curves of the Fe-Zn-SA/NC show a higher reduction current density in an O_2-saturated electrolyte, implying an outstanding ORR performance of this catalyst. As presented in Fig. 3(a), the LSV of Fe-Zn-SA/NC demonstrates a more positive onset potential (E_{onset}, 0.87 V vs. RHE), half-wave potential ($E_{1/2}$, 0.78 V vs. RHE), and larger diffusion-limited current density (J_L, 4.72 mA·cm^{-2}). These values are very close to those of commercial Pt/C catalyst (E_{onset}, 0.94 V, $E_{1/2}$, 0.80 V, J_L, 5.06 mA·cm^{-2}) and even higher than most of the recent reports (Table S1 in the ESM). Notably, Fe-Zn-SA/NC also exhibits obvious enhanced ORR performance compared to Fe-SA/NC and Zn-SA/NC catalysts. It indicates that the catalytic activity derives from the synergistic effect of Fe-Zn atomic pairs is far

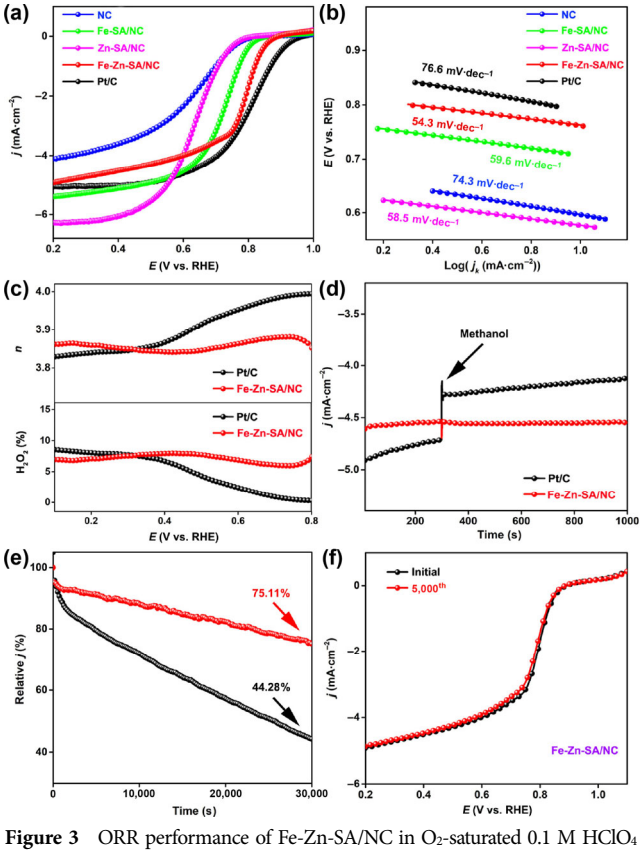

Figure 3 ORR performance of Fe-Zn-SA/NC in O_2-saturated 0.1 M $HClO_4$ solution. (a) ORR polarization curves for different catalysts in 0.1 M $HClO_4$ solution. (b) Tafel plots of Fe-Zn-SA/NC, Fe-SA/NC, Zn-SA/NC and Pt/C catalysts. (c) Electron transfer number and H_2O_2 yield plots of Fe-Zn-SA/NC and Pt/C. (d) Chronoamperometric curves of a methanol crossover test with Fe-Zn-SA/NC and Pt/C at 0.3 V vs. RHE. (e) The amperometric *i*–*t* response to the Fe-Zn-SA/NC and Pt/C at 0.7 V vs. RHE. (f) ORR polarization curves before and after 5,000 CV cycles over Fe-Zn-SA/NC electrocatalyst.

greater than those of Fe single atoms or Zn single atoms towards ORR. The Tafel slopes were derived to evaluate the ORR kinetic character of Fe-Zn-SA/NC and Pt/C. As shown in Fig. 3(b), Fe-Zn-SA/NC exhibits smaller Tafel slopes (54.3 mV·dec^{-1}) than that of the Pt/C (76.6 mV·dec^{-1}) in acidic conditions, indicating an accelerated ORR kinetic of Fe-Zn-SA/NC [48], also suggesting the migration of adsorbed oxygen intermediates is more likely to be the rate-determining step for Fe-Zn-SA/NC and Pt/C [49, 50]. Further, the ECSA of the samples were also evaluated by measuring electrochemical double-layer capacitances (C_{dl}) (Fig. S12 in the ESM) [51, 52]. As shown in Fig. S13 in the ESM, the C_{dl} value of Fe-Zn-SA/NC is 70.0 mF·cm^{-2}, higher than those of reference materials, further indicative of the increased electrochemically active sites of Fe-Zn-SA/NC. Besides, EIS tests of Fe-Zn-SA/NC and reference materials were conducted. As depicted in Fig. S14 in the ESM, Fe-Zn-SA/NC has the best electron transfer ability among the samples, agreeing with its optimal ORR activity.

The K-L plots in Fig. S15 in the ESM show good linearity, elucidating the first-order reaction kinetics of Fe-Zn-SA/NC [22]. The electron transfer number (n) for Fe-Zn-SA/NC is calculated by the RRDE measurements in Fig. 3(c). In the potential range between 0.1 and 0.8 V, the n value of Fe-Zn-SA/NC is 3.86–3.88, and the H_2O_2 yield remains below 8%, further suggesting that the Fe-Zn-SA/NC possesses a direct four-electron ($4e^-$) pathway [48]. In addition, ORR is an important catalytic reaction applied to methanol fuel cells, we also performed the methanol crossover test of the catalysts as displayed in Fig. 3(d). In comparison with the sharply decreased current density of Pt/C after injecting methanol (3 M/L), the current density of Fe-Zn-SA/NC just shows a partial delay, reflecting its excellent methanol tolerance. The long-time stability of Fe-Zn-SA/NC was evaluated. It's worth noting that the current density of commercial Pt/C degrades rapidly in acidic electrolyte, and its stability is inferior to that in alkaline or neutral electrolyte [53, 54]. As depicted in Fig. 3(e), after 30,000 s long-time tests, Fe-Zn-SA/NC exhibits a lower current decay compared to Pt/C, indicating its better ORR stability. In addition, after 5,000 CV scans in 0.1 M $HClO_4$ under the O_2-atmosphere (Fig. 3(f)), the $E_{1/2}$ of the Fe-Zn-SA/NC shows no obvious decrease, further indicating the good stability of the catalyst in acidic conditions.

In this work, we also investigated the ORR performance of Fe-Zn-SA/NC in alkaline (0.1 M KOH) and neutral (0.1 M PBS) conditions. The CV curves of the Fe-Zn-SA/NC show a higher reduction current density in an O_2-saturated electrolyte than that in N_2-saturated ones, both in alkaline and neutral conditions as observed in Fig. S16 in the ESM. As shown in Figs. 4(a) and 4(b), Fe-Zn-SA/NC holds a good ORR activity with a large positive $E_{1/2}$ of 0.85 V in alkaline media and 0.72 V in neutral media, which is comparable to the Pt/C (0.83 V in alkaline media and 0.72 V in neutral media) and most of the recent reports (Tables S2 and S3 in the ESM). Furthermore, as shown in Figs. 4(c) and 4(d), Fe-Zn-SA/NC also exhibits small Tafel slopes in both alkaline (41.7 mV·dec^{-1}) and neutral conditions (112.6 mV·dec^{-1}), indicating the superior reaction kinetics of Fe-Zn-SA/NC. Similarly, in alkaline solution, the rate-determining step of Pt/C is probably the migration of adsorbed oxygen intermediates, while rate-determining step of Fe-Zn-SA/NC comes to be the protonation of *O intermediate. However, in neutral solution, the first electron transfer step comes the rate-determining step of ORR for Fe-Zn-SA/NC and Pt/C [49, 50, 55]. According to K-L equation (Figs. S17 and S18 in the ESM), the calculated electrode transfer number

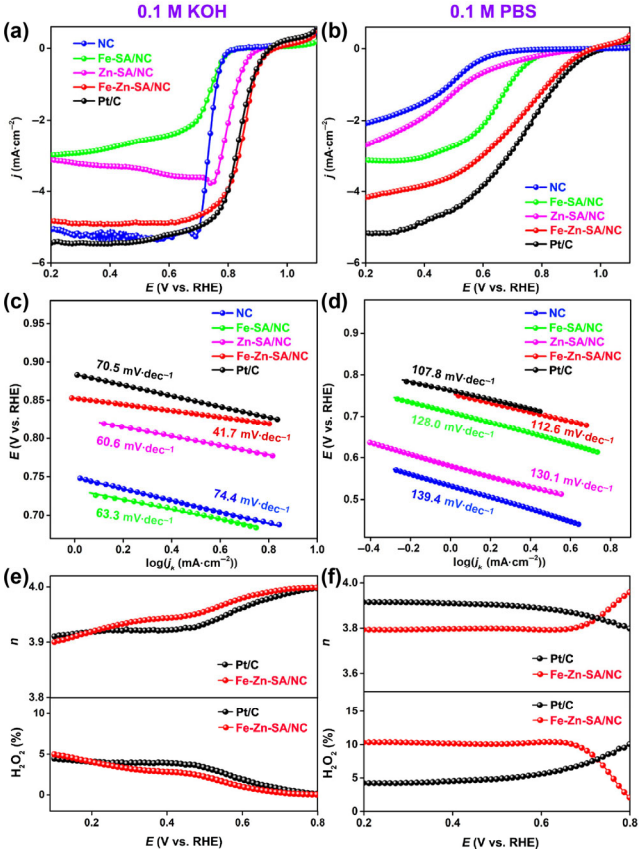

Figure 4 ORR performance of Fe-Zn-SA/NC in O_2-saturated 0.1 M KOH and PBS solutions. (a) and (b) ORR polarization curves for different catalysts. (c) and (d) Tafel plots of Fe-Zn-SA/NC, Fe-SA/NC, Zn-SA/NC and Pt/C. (e) and (f) Electron transfer number and H_2O_2 yield plots of Fe-Zn-SA/NC and Pt/C.

was close to 4. The n and H_2O_2 yield were further evaluated (Figs. 4(e) and 4(f) using the RRDE. In alkaline electrolyte, the n and H_2O_2 yield are determined to be 3.90–4.00 and 5%, respectively; while in neutral media, they are about 3.80–3.96 and 10%, respectively. Therefore, ORR on Fe-Zn-SA/NC follows a near $4e^-$ transfer pathway in both alkaline and neutral conditions, demonstrating an efficient reduction of O_2. In addition, Fe-Zn-SA/NC also shows excellent methanol tolerance in alkaline and neutral conditions (Fig. S19 in the ESM), convincingly implying a favorable tolerance toward the small organic molecules. Furthermore, the long-time stability tests of Fe-Zn-SA/NC in alkaline and neutral conditions (Figs. S20 and S21 in the ESM) also suggest the excellent stability of Fe-Zn-SA/NC toward ORR. After the long-term catalysis procedure, no obvious change appears in the structure and morphology of Fe-Zn-SA/NC, as indicated by XRD pattern, XPS spectrum and HAADF-STEM image results (Figs. S22–S24 in the ESM). The metal species still exist as single atoms after long-term testing. These results reveal the excellent long-term stability of Fe-Zn-SA/NC during electrochemical operation. Further, the ORR tests of Fe-SA/NC and Zn-SA/NC were also performed in acidic, alkaline and neutral electrolytes under the same conditions as those of Fe-Zn-SA/NC (Figs. S25–S27 in the ESM). All results show that the ORR catalytic activity of Fe-Zn atomic pairs is superior to that of Fe or Zn single-atom sites. Besides, after normalizing their activity against the amount of metals, Fe-Zn-SA/NC shows the best mass activity of 0.86, 2.01, and 0.61 mA·mg^{-1} at 0.8 V vs. RHE in acidic, alkaline and neutral conditions, respectively (Fig. S28 in the ESM), highlighting the wonderful ORR catalytic activity of Fe-Zn-SA/NC.

To evaluate the practical application of Fe-Zn-SA/NC electrocatalyst in energy conversion storage devices, a primary Zn-air battery was assembled utilizing Fe-Zn-SA/NC as the air cathodes and 6.0 M KOH as electrolyte [56, 57]. As depicted in Fig. 5(a), the maximum power density of the Fe-Zn-SA/NC was up to 167.2 mW·cm^{-2}, which close to 169.3 mW·cm^{-2} of Pt/C. The open-circuit voltage of the Fe-Zn-SA/NC was as large as ~ 1.44 V (insert of Fig. 5(b)). Moreover, the Fe-Zn-SA/NC based Zn-air battery delivers a specific capacity of 756.6 mAh·g$_{Zn}^{-1}$ at 10 mA·cm^{-2}, corresponding to a ~ 92.3% utilization of the theoretical capacity (~ 820 mAh·g$_{Zn}^{-1}$) (Fig. 5(b)). In addition, Fe-Zn-SA/NC was assembled into a primary Zn-air battery of neutral electrolyte (Fig. S29 in the ESM), which also shows a satisfying performance. Furthermore, when assembled as an alkaline rechargeable Zn-air battery by utilizing Fe-Zn-SA/NC+IrO_2 as the air cathodes, it displays outstanding cycling stability as indicated by a negligible voltage variation for continuous 360 cycles (120 h) in Fig. 5(c), whereas Pt/C + IrO_2 based rechargeable Zn-air battery shows an unacceptable rise of the voltage gap between charge and discharge after 135 cycles due to the gradually inactivated Pt/C and IrO_2 catalysts. The good performance and impressive operation durability of the rechargeable Zn-air battery reveal the feasibility of Fe-Zn-SA/NC electrocatalyst in real energy-related devices.

To determine the intrinsic reason for the better ORR performance of Fe-Zn-SA/NC compared with Fe-SA/NC and Zn-SA/NC, the DFT calculations were explored from the thermodynamics. As presented in Fig. 6(a), the O_2 molecule can be chemically adsorbed on the Fe-Zn-N_6, Fe-N_4 and Zn-N_4 sites with pre-adsorbed OH radicals, while tending to be physically adsorbed on the Zn-N_4 site, showing a relatively weak reaction possibility. It is worthy to note that the O–O bond of O_2 is slightly elongated to 1.293 Å after adsorption on Fe-Zn-N_6(2OH) sites, in contrast, the O–O bond is 1.290 and 1.240 Å when O_2 was adsorbed on Fe-N_4(OH) and Zn-N_4(OH) sites, respectively. The big difference may be derived from the differentiated modulation of the electronic structures by surrounding coordination atoms (Fe, Zn and N). The elongated O–O bond on Fe-Zn-N_6(2OH) sites would promote

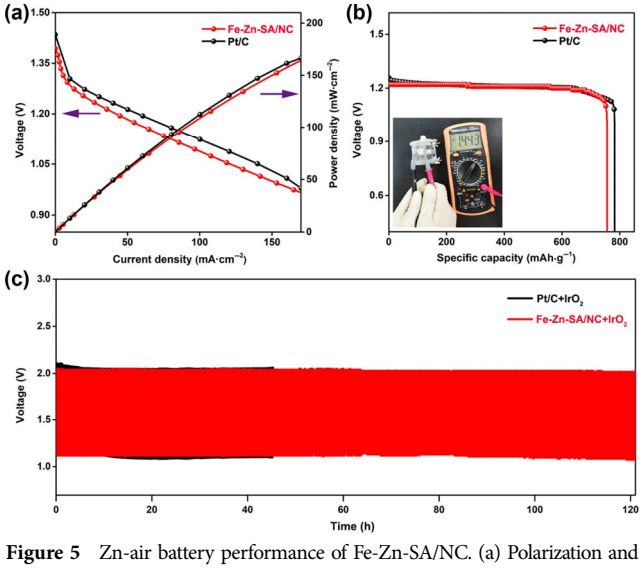

Figure 5 Zn-air battery performance of Fe-Zn-SA/NC. (a) Polarization and power density curves of primary Zn-air battery using Fe-Zn-SA/NC or Pt/C as ORR catalyst in 6 M KOH electrolyte. (b) Long-time galvanostatic discharge curves of a Zn-air battery with Fe-Zn-SA/NC or Pt/C as cathode catalyst until complete consumption of Zn anode and the inset is the photograph of open-circuit voltage. (c) Long-term galvanostatic discharge-charge plots at 10 mA·cm^{-2}.

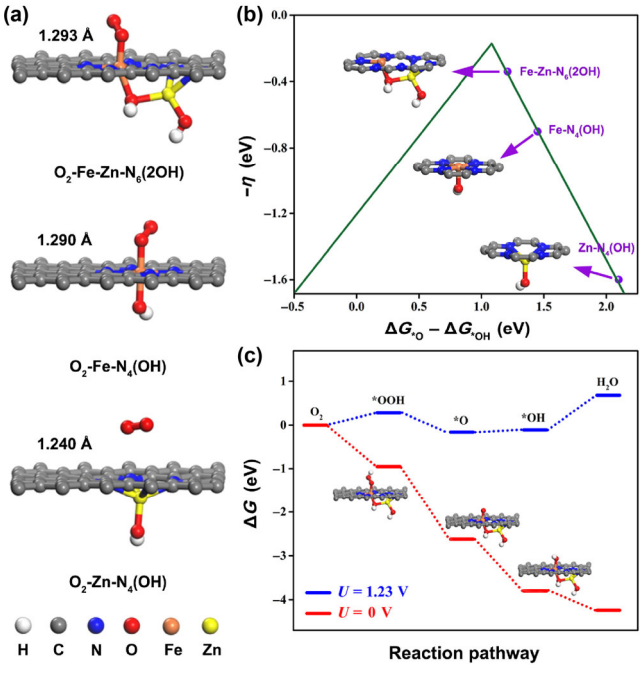

Figure 6 DFT calculations. (a) Optimized geometries of O_2 on the Fe-Zn-N_6, Fe-N_4, and Zn-N_4 with pre-adsorbed OH systems. (b) Volcano plot for the ORR overpotential against the standard free energy of $\Delta G_{*O} - \Delta G_{*OH}$. (c) Free energy profiles for ORR at U = 0 and 1.23 V (the equilibrium potential for a 4e^- ORR) on Fe-Zn-SA/NC with the possible pathways. The insets in c are the most stable configurations of *OOH, *O and *OH intermediates obtained by the DFT calculations.

the hydrogenation of O_2 and reduce the O–OH dissociation energy barrier [24], thus efficiently enhancing the ORR activity. Furthermore, the oxygen-containing intermediates of *O and *OH, which play significant roles in the ORR reaction, could be used as the descriptors. The adsorption free energies of *O and *OH are calculated via considering possible initial configurations [58]. As shown in the ORR volcano plot (Fig. 6(b)), the free energy differences of ($\Delta G_{*O} - \Delta G_{*OH}$) were adopted as the descriptor to screen the ORR activities for various catalysts. It can be seen that the Fe-Zn-N_6(2OH) shows the best ORR performance with the location close to the apex of the volcano, while Fe-N_4(OH) and Zn-N_4(OH) are away from the volcano peak. In addition, we further investigated the possible ORR reaction pathways on Fe-Zn-SA/NC at U = 0 and 1.23 V in Fig. 6(c). The possible reaction pathways for ORR is O_2→*OOH→*O→*OH→ H_2O, following a 4e^- transfer pathway [34]. This reaction mechanism clearly shows that the energy barrier is easy to overcome when U = 1.23 V due to the low potential determining step from the thermodynamical perspective. These DFT results are also in good agreement with our experimental results, which further indicates that our synthesized Fe-Zn atomic pair catalyst has high ORR activity.

4 Conclusions

In summary, we prepared atomically dispersed Fe-Zn pairs anchored on porous N-doped carbon frameworks by a simple calcination method. The as-synthesized isolated Fe-Zn atomic pairs are accurately identified through the EELS technologies, and Fe-Zn atomic pairs are determined to be bonded with six pyridinic-N atoms from XAFS characterization. The synergistic effect between the isolated Fe-Zn atoms pairs and nitrogen coordinated Fe or Zn single atoms (Fe-Zn-N_6, Fe-N_4, Zn-N_4) promotes the ORR activities. The porous N-doped carbon matrix ensures abundant exposed active sites and efficient transfer of

the ORR-related electrons. As a result, Fe-Zn-SA/NC affords excellent ORR activities in the whole pH range. Furthermore, the good performance and impressive durability of Zn-air battery reveal the feasibility of Fe-Zn-SA/NC electrocatalyst in real energy-related devices. DFT calculations demonstrate that the relatively lower energy barriers on the Fe-Zn-N_6 centers contribute to its higher ORR catalytic activity. This work demonstrates the potential of Fe-Zn pairs as an alternative to the Pt catalysts for efficient all-pH ORR and provides new opportunities for the rational design and construction of other multifunctional dual-atom catalysts for diverse applications.

Acknowledgements

This work was financially supported by the National Key R&D Program of China (No. 2017YFA0700104), the National Natural Science Foundation of China (Nos. 22075211, 21601136, 51971157, 51761165012, and 62005173), Project funded by China Postdoctoral Science Foundation (No. 2020TQ0201), Tianjin Science Fund for Distinguished Young Scholars (No. 19JCJQJC61800). The authors also acknowledge National Supercomputing Center in Shenzhen for providing the computational resources and materials studio (version 7.0, DMol^3).

Electronic Supplementary Material: Supplementary material (TEM and STEM images, Raman, XPS and EELS spectra, and electrocatalytic measurements) is available in the online version of this article at https://doi.org/10.1007/s12274-020-3186-x.

References

[1] Qu, Y. T.; Li, Z. J.; Chen, W. X.; Lin, Y.; Yuan, T. W.; Yang, Z. K.; Zhao, C. M.; Wang, J.; Zhao, C.; Wang, X. et al. Direct transformation of bulk copper into copper single sites via emitting and trapping of atoms. *Nat. Catal.* **2018**, *1*, 781–786.

[2] Zhang, J. Q.; Zhao, Y. F.; Chen, C.; Huang, Y. C.; Dong, C. L.; Chen, C. J.; Liu, R. S.; Wang, C. Y.; Yan, K.; Li, Y. D. et al. Tuning the coordination environment in single-atom catalysts to achieve highly efficient oxygen reduction reactions. *J. Am. Chem. Soc.* **2019**, *141*, 20118–20126.

[3] Tang, C.; Jiao, Y.; Shi, B. Y.; Liu, J. N.; Xie, Z. H.; Chen, X.; Zhang, Q.; Qiao, S. Z. Coordination tunes selectivity: Two-electron oxygen reduction on high-loading molybdenum single-atom catalysts. *Angew. Chem., Int. Ed.* **2020**, *132*, 9256–9261.

[4] Wan, C. Z.; Duan, X. F.; Huang, Y. Molecular design of single-atom catalysts for oxygen reduction reaction. *Adv. Energy Mater.* **2020**, *10*, 1903815.

[5] Hu, B. C.; Wu, Z. Y.; Chu, S. Q.; Zhu, H. W.; Liang, H. W.; Zhang, J.; Yu, S. H. SiO_2-protected shell mediated templating synthesis of Fe-N-doped carbon nanofibers and their enhanced oxygen reduction reaction performance. *Energy Environ. Sci.* **2018**, *11*, 2208–2215.

[6] Li, Q. H.; Chen, W. X.; Xiao, H.; Gong, Y.; Li, Z.; Zheng, L. R.; Zheng, X. S.; Yan, W. S.; Cheong, W. C.; Shen, R. A. et al. Fe isolated single atoms on S, N codoped carbon by copolymer pyrolysis strategy for highly efficient oxygen reduction reaction. *Adv. Mater.* **2018**, *30*, 1800588.

[7] Yan, D. F.; Li, Y. X.; Huo, J.; Chen, R.; Dai, L. M.; Wang, S. Y. Defect chemistry of nonprecious-metal electrocatalysts for oxygen reactions. *Adv. Mater.* **2017**, *29*, 1606459.

[8] Zhou, D. J.; Cai, Z.; Lei, X. D.; Tian, W. L.; Bi, Y. M.; Jia, Y.; Han, N. N.; Gao, T. F.; Zhang, Q.; Kuang, Y. et al. NiCoFe-layered double hydroxides/N-doped graphene oxide array colloid composite as an efficient bifunctional catalyst for oxygen electrocatalytic reactions. *Adv. Energy Mater.* **2018**, *8*, 1701905.

[9] Bu, L. Z.; Zhang, N.; Guo, S. J.; Zhang, X.; Li, J.; Yao, J. L.; Wu, T.; Lu, G.; Ma, J. Y.; Su, D. et al. Biaxially strained PtPb/Pt core/shell nanoplate boosts oxygen reduction catalysis. *Science* **2016**, *354*, 1410–1414.

[10] Bu, L. Z.; Shao, Q.; E, B.; Guo, J.; Yao, J. L.; Huang, X. Q. PtPb/PtNi intermetallic core/atomic layer shell octahedra for efficient oxygen reduction electrocatalysis. *J. Am. Chem. Soc.* **2017**, *139*, 9576–9582.

[11] Gu, W. L.; Hu, L. Y.; Li, J.; Wang, E. K. Hybrid of g-C_3N_4 assisted metal−organic frameworks and their derived high-efficiency oxygen reduction electrocatalyst in the whole pH range. *ACS Appl. Mater. Interfaces* **2016**, *8*, 35281−35288.

[12] Li, X. Y.; Rong, H. P.; Zhang, J. T.; Wang, D. S.; Li, Y. D. Modulating the local coordination environment of single-atom catalysts for enhanced catalytic performance. *Nano Res.* **2020**, *13*, 1842–1855.

[13] Ji, S. F.; Chen, Y. J.; Wang, X. L.; Zhang, Z. D.; Wang, D. S.; Li, Y. D. Chemical synthesis of single atomic site catalysts. *Chem. Rev.*, in press, DOI: 10.1021/acs.chemrev.9b00818.

[14] Xiong, Y.; Dong, J. C.; Huang, Z. Q.; Xin, P. Y.; Chen, W. X.; Wang, Y.; Li, Z.; Jin, Z.; Xing, W.; Zhuang, Z. B. et al. Single-atom Rh/N-doped carbon electrocatalyst for formic acid oxidation. *Nat. Nanotechnol.* **2020**, *15*, 390–397.

[15] Zhang, N. Q.; Ye, C. L.; Yan, H.; Li, L. C.; He, H.; Wang, D. S.; Li, Y. D. Single-atom site catalysts for environmental catalysis. *Nano Res.* **2020**, *13*, 3165–3182.

[16] Zhang, C. H.; Sha, J. W.; Fei, H. L.; Liu, M. J.; Yazdi, S.; Zhang, J. B.; Zhong, Q. F.; Zou, X. L.; Zhao, N. Q.; Yu, H. S. et al. Single-atomic ruthenium catalytic sites on nitrogen-doped graphene for oxygen reduction reaction in acidic medium. *ACS Nano* **2017**, *11*, 6930–6941.

[17] Xue, J. L.; Li, Y. S.; Hu, J. Nanoporous bimetallic Zn/Fe–N–C for efficient oxygen reduction in acidic and alkaline media. *J. Mater. Chem. A* **2020**, *8*, 7145–7157.

[18] Huo, J. J.; Lu, L.; Shen, Z. Y.; Liu, Y.; Guo, J. J.; Liu, Q. B.; Wang, Y.; Liu, H.; Wu, M. H.; Wang, G. X. A rational synthesis of single-atom iron-nitrogen electrocatalysts for highly efficient oxygen reduction reaction. *J. Mater. Chem. A* **2020**, *8*, 16271–16282.

[19] Yang, H. Q.; Li, Z. Y.; Kou, S. Q.; Lu, G. L.; Liu, Z. N. A complex-sequestered strategy to fabricate Fe single-atom catalyst for efficient oxygen reduction in a broad pH-range. *Appl. Catal. B Environ.* **2020**, *278*, 119270.

[20] Wang, X.; Jia, Y.; Mao, X.; Liu, D. B.; He, W. X.; Li, J.; Liu, J. G.; Yan, X. C.; Chen, J.; Song, L. et al. Edge-rich Fe–N_4 active sites in defective carbon for oxygen reduction catalysis. *Adv. Mater.* **2020**, *32*, 2000966.

[21] Shang, H. S.; Zhou, X. Y.; Dong, J. C.; Li, A.; Zhao, X.; Liu, Q. H.; Lin, Y.; Pei, J. J.; Li, Z.; Jiang, Z. L. et al. Engineering unsymmetrically coordinated Cu-S_1N_3 single atom sites with enhanced oxygen reduction activity. *Nat. Commun.* **2020**, *11*, 3049.

[22] Wang, X. L.; Du, J.; Zhang, Q. H.; Gu, L.; Cao, L. J.; Liang, H. P. *In situ* synthesis of sustainable highly efficient single iron atoms anchored on nitrogen doped carbon derived from renewable biomass. *Carbon* **2020**, *157*, 614–621.

[23] Sun, T. T.; Li, Y. L.; Cui, T. T.; Xu, L. B.; Wang, Y G.; Chen, W. X.; Zhang, P. P.; Zheng T. Y.; Fu, X. Z.; Zhang, S. L. et al. Engineering of coordination environment and multiscale structure in single-site copper catalyst for superior electrocatalytic oxygen reduction. *Nano Lett.* **2020**, *20*, 6206–6214.

[24] Sun, T. T.; Xu, L. B.; Wang, D. S.; Li, Y. D. Metal organic frameworks derived single atom catalysts for electrocatalytic energy conversion. *Nano Res.* **2019**, *12*, 2067–2080.

[25] Chen, Y.; Guo, R. J.; Peng, X. Y.; Wang, X. Q.; Liu, X. J.; Ren, J. Q.; He, J.; Zhuo, L. C.; Sun, J. Q.; Liu, Y. F. et al. Highly productive electrosynthesis of ammonia by admolecule-targeting single Ag sites. *ACS Nano* **2020**, *14*, 6938–6946.

[26] Peng, X. Y.; Zhao, S. Z.; Mi, Y. Y.; Han, L. L.; Liu, X. J.; Qi, D. F.; Sun, J. Q.; Liu, Y. F.; Bao, H. H.; Zhuo, L. C. et al. Trifunctional single-atomic Ru sites enable efficient overall water splitting and oxygen reduction in acidic media. *Samll* **2020**, *16*, 2002888.

[27] Zhou, H.; Zhao, Y. F.; Xu, J.; Sun, H. R.; Li, Z. J.; Liu, W.; Yuan, T. W.; Liu, W.; Wang, X. Q.; Cheong, W. C. et al. Recover the activity of sintered supported catalysts by nitrogen-doped carbon atomization. *Nat. Commun.* **2020**, *11*, 335.

[28] Zhuang, Z. C.; Kang, Q.; Wang, D. S.; Li, Y. D. Single-atom catalysis enables long-life, high-energy lithium-sulfur batteries. *Nano Res.* **2020**, *13*, 1856–1866.

[29] Zhang, H. B.; An, P. F.; Zhou, W.; Guan, B. Y.; Zhang, P.; Dong, J. C.; Lou, X. W. Dynamic traction of lattice-confined platinum atoms

into mesoporous carbon matrix for hydrogen evolution reaction. *Sci. Adv*. **2018**, *4*, eaao6657.

[30] Lü, F.; Zhao, S. Z.; Guo, R. J.; He, J.; Peng, X. Y.; Bao, H. H.; Fu, J. T.; Han, L. L.; Qi, G. C.; Luo, J. et al. Nitrogen-coordinated single Fe sites for efficient electrocatalytic N_2 fixation in neutral media. *Nano Energy* **2019**, *61*, 420–427.

[31] Shang, H. S.; Jiang, Z. L.; Zhou, D. N.; Pei, J. J.; Wang, Y.; Dong, J. C.; Zheng, X. S.; Zhang, J. T.; Chen, W. X. Engineering a metal-organic framework derived Mn-N_4-C_xS_y atomic interface for highly efficient oxygen reduction reaction. *Chem. Sci*. **2020**, *11*, 5994–5999.

[32] Shang, H. S.; Sun, W. M.; Sui, R.; Pei, J. J.; Zheng, L. R.; Dong, J. C.; Jiang, Z. L.; Zhou, D. N.; Zhuang, Z. B.; Chen, W. X. et al. Engineering isolated Mn–N_2C_2 atomic interface sites for efficient bifunctional oxygen reduction and evolution reaction. *Nano Lett*. **2020**, *20*, 5443–5450.

[33] Yu, L. J.; Yang, C. C.; Zhang, W. D.; Liu, W. Q.; Wang, H. F.; Qi, J. W.; Xu, L. Solvent-free synthesis of N-doped nanoporous carbon materials as durable high-performance pH-universal ORR catalysts. *J. Colloid Interface Sci*. **2020**, *575*, 406–415.

[34] Lu, Z. Y.; Wang, B.; Hu, Y. F.; Liu, W.; Zhao, Y. F.; Yang, R. O.; Li, Z. P.; Luo, J.; Chi, B.; Jiang, Z. et al. An isolated zinc–cobalt atomic pair for highly active and durable oxygen reduction. *Angew. Chem., Int. Ed*. **2019**, *58*, 2622–2626.

[35] Wang, J.; Huang, Z. Q.; Liu, W.; Chang, C. R.; Tang, H. L.; Li, Z. J.; Chen, W. X.; Jia, C. J.; Yao, T.; Wei, S. Q. et al. Design of N-coordinated dual-metal sites: A stable and active Pt-free catalyst for acidic oxygen reduction reaction. *J. Am. Chem. Soc*. **2017**, *139*, 17281–17284.

[36] Wang, Y. Y.; Zhang, G. X.; Ma, M.; Ma, Y.; Huang, J. K.; Chen, C.; Zhang, Y.; Sun, X. M.; Yan, Z. F. Ultrasmall NiFe layered double hydroxide strongly coupled on atomically dispersed FeCo-NC nanoflowers as efficient bifunctional catalyst for rechargeable Zn-air battery. *Sci. China Mater*. **2020**, *63*, 1182–1195.

[37] Han, L. L.; Song, S. J.; Liu, M. J.; Yao, S. Y.; Liang, Z. X.; Cheng, H.; Ren, Z. H.; Liu, W.; Lin, R. Q.; Qi, G. C. et al. Stable and efficient single-atom Zn catalyst for CO_2 reduction to CH_4. *J. Am. Chem. Soc*. **2020**, *142*, 12563–12567.

[38] Wang, H. B.; Maiyalagan, T.; Wang, X. Review on recent progress in nitrogen-doped graphene: Synthesis, characterization, and its potential applications. *ACS Catal*. **2012**, *2*, 781–794.

[39] Xu, J.; Lai, S. H.; Hu, M.; Ge, S. M.; Xie, R. C.; Li, F.; Hua, D. D.; Xu, H.; Zhou, H.; Wu, R. et al. Semimetal 1H-SnS_2 enables high-efficiency electroreduction of CO_2 to CO. *Small Methods* **2020**, *4*, 2000567.

[40] Liu, W.; Han, L. L.; Wang, H. T.; Zhao, X. R.; Boscoboinik, J. A.; Liu, X. J.; Pao, C. W.; Sun, J. Q.; Zhuo, L. C.; Luo, J. et al. FeMo sub-nanoclusters/single atoms for neutral ammonia electrosynthesis. *Nano Energy* **2020**, *77*, 105078.

[41] Xu, J.; He, J.; Ding, Y.; Luo, J. X-ray imaging of atomic nuclei. *Sci. China Mater*. **2020**, *63*, 1788–1796.

[42] Gloter, A.; Ingrin, J.; Bouchet, D.; Colliex, C. Composition and orientation dependence of the O *K* and Fe $L_{2,3}$ EELS fine structures in $Ca_2(Al_xFe_{1-x})_2O_5$. *Phys. Rev. B* **2000**, *61*, 2587–2594.

[43] Guinel, M. J. F.; Brodusch, N.; Sha, G.; Shandiz, M. A.; Demers, H.; Trudeau, M.; Ringer, S. P.; Gauvin, R. Microscopy and microanalysis of complex nanosized strengthening precipitates in new generation commercial Al-Cu-Li alloys. *J. Microsc*. **2014**, *255*, 128–137.

[44] Liu, D.; Li, J. C.; Ding, S. C.; Lyu, Z. Y.; Feng, S.; Tian, H. Y.; Huyan, C. X.; Xu, M. J.; Li, T.; Du, D. et al. 2D single-atom catalyst with optimized iron sites produced by thermal melting of metal–organic frameworks for oxygen reduction reaction. *Small Methods* **2020**, *4*, 1900827.

[45] Zhang, Z. P.; Sun, J. T.; Wang, F.; Dai, L. M. Efficient oxygen reduction reaction (ORR) catalysts based on single iron atoms dispersed on a hierarchically structured porous carbon framework. *Angew. Chem., Int. Ed*. **2018**, *57*, 9038–9043.

[46] Yin, P. Q.; Yao, T.; Wu, Y. E.; Zheng, L. R.; Lin, Y.; Liu, W.; Ju, H. X.; Zhu, J. F.; Hong, X.; Deng, Z. X. et al. Single cobalt atoms with precise N-coordination as superior oxygen reduction reaction catalysts. *Angew. Chem., Int. Ed*. **2016**, *55*, 10800–10805.

[47] Yang, F.; Song, P.; Liu, X. Z.; Mei, B. B.; Xing, W.; Jiang, Z.; Gu, L.; Xu, W. L. Highly efficient CO_2 electroreduction on ZnN_4-based single-atom catalyst. *Angew. Chem., Int. Ed*. **2018**, *57*, 12303–12307.

[48] Chen, G. B.; Liu, P.; Liao, Z. Q.; Sun, F. F.; He, Y. H.; Zhong, H. X.; Zhang, T.; Zschech, E.; Chen, M. W.; Wu, G. et al. Zinc-mediated template synthesis of Fe-N-C electrocatalysts with densely accessible Fe-N_x active sites for efficient oxygen reduction. *Adv. Mater*. **2020**, *32*, 1907399.

[49] Sun, J. Q.; Lowe, S. E.; Zhang, L. J.; Wang, Y. Z.; Pang, K. L.; Wang, Y.; Zhong, Y. L.; Liu, P. R.; Zhao, K.; Tang, Z. Y. et al. Ultrathin nitrogen-doped holey carbon@graphene bifunctional electrocatalyst for oxygen reduction and evolution reactions in alkaline and acidic media. *Angew. Chem., Int. Ed*. **2018**, *57*, 16511–16515.

[50] Wu, G.; Cui, G. F.; Li, D. Y.; Shen, P. K.; Li, N. Carbon-supported $Co_{1.67}Te_2$ nanoparticles as electrocatalysts for oxygenreduction reaction in alkaline electrolyte. *J. Mater. Chem*. **2009**, *19*, 6581–6589.

[51] Xu, J.; Zhang, C. X.; Liu, H. X.; Sun, J. Q.; Xie, R. C.; Qiu, Y.; Lü, F.; Liu, Y. F.; Zhuo, L. C.; Liu, X. J. et al. Amorphous MoO_x-stabilized single platinum atoms with ultrahigh mass activity for acidic hydrogen evolution. *Nano Energy* **2020**, *70*, 104529.

[52] Wang, Y.; Chen, A. R.; Lai, S. H.; Peng, X. Y.; Zhao, S. Z.; Hu, G. Z.; Qiu, Y.; Ren, J. Q.; Liu, X. J.; Luo, J. Self-supported $NbSe_2$ nanosheet arrays for highly efficient ammonia electrosynthesis under ambient conditions. *J. Catal*. **2020**, *381*, 78–83.

[53] Wang, S. P.; Zhu, M. L.; Bao, X. B.; Wang, J.; Chen, C. H.; Li, H. R.; Wang, Y. Synthesis of mesoporous Fe–N/C materials with high catalytic performance in the oxygen reduction reaction. *ChemCatChem* **2015**, *7*, 2937–2944.

[54] Liu, J.; Yin, J.; Feng, B.; Li, F.; Wang, F. One-pot synthesis of unprotected PtPd nanoclusters with enhanced catalytic activity, durability, and methanol-tolerance for oxygen reduction reaction. *Appl. Surf. Sci*. **2019**, *473*, 318–325.

[55] Shinagawa, T.; Garcia-Esparza, A. T.; Takanabe, K. Insight on Tafel slopes from a microkinetic analysis of aqueous electrocatalysis for energy conversion. *Sci. Rep*. **2015**, *5*, 13801.

[56] Wan, W. J.; Liu, X. J.; Li, H. Y.; Peng, X. Y.; Xi, D. S.; Luo, J. 3D carbon framework-supported CoNi nanoparticles as bifunctional oxygen electrocatalyst for rechargeable Zn-air batteries. *Appl. Catal. B Environ*. **2019**, *240*, 193–200.

[57] Li, H. Y.; Wan, W. J.; Liu, X. J.; Liu, H. X.; Shen, S. B.; Lv, F.; Luo, J. Poplar-catkin-derived N, P-Co-doped carbon microtubes as efficient oxygen electrocatalysts for Zn–air batteries. *ChemElectroChem* **2018**, *5*, 1113–1119.

[58] Sun, Y. L.; Wang, J.; Liu, Q.; Xia, M. R.; Tang, Y. F.; Gao, F. M.; Hou, Y. L.; Tse, J.; Zhao, Y. F. Itinerant ferromagnetic half metallic cobalt–iron couples: Promising bifunctional electrocatalysts for ORR and OER. *J. Mater. Chem. A* **2019**, *7*, 27175–27185.